Numerical simulation of mixed mode (I and II) fracture behavior of pre-cracked rock using the strong discontinuity approach

M. H. Motamedi[a], D. A. Weed[a], C. D. Foster[a,*]

[a]*Department of Civil and Materials Engineering, University of Illinois at Chicago, Chicago, IL, USA*

Abstract

The existence of macroscopic flaws in geomaterial structures profoundly influences their load-carrying capacity and failure patterns. This paper is devoted to the numerical investigation of mixed mode fracture propagation in a cracked Brazilian disk (CBD) specimen by means of the embedded strong discontinuity approach (SDA). A recently modified nonassociated, three-invariant cap plasticity model with mixed isotropic/kinematic hardening is used to predict the continuum response for the intact part of the specimen. In addition, this constitutive model adopts bifurcation analysis to track the inception of new localization and crack path propagation. For the post-localization regime, a cohesive-law fracture model, able to address mixed-model failure condition, is implemented to characterize the constitutive softening behavior on the surface of discontinuity. To capture propagating fracture, the Assumed Enhanced Strain (AES) method is employed. Furthermore, particular mathematical treatments are incorporated into the simulation concerning numerical efficiency and robustness issues. Finally, the results obtained from the enhanced FE simulations are analyzed and critically compared with experimental results available in the literature.

Keywords: Fracture; Strong discontinuities; Cap plasticity; Bifurcation analysis; Crack propagation

*Corresponding author. Tel.: +1-312-996-8086, Fax:+1-312-996-2426.
Email address: fosterc@uic.edu (C. D. Foster)

1. Introduction

Numerical simulation of geotechnical and geological structures, especially in the platform of the finite element (FE) method, has attracted much research interest with the advent of modern computational resources. One crucial part of an FE simulation is the selection of an appropriate constitutive material model, since geomaterials can exhibit many complex and interacting behaviors. At low confining pressure, localized deformation in the form of shear and/or dilation bands or fractures may occur due to the growth and coalescence of micro-cracks and pores. At high confining pressure, on the contrary, delocalized irreversible deformation may occur in the form of shear-enhanced compaction. The latter response, generally accompanied by material hardening, is the result of pore collapse, grain crushing, internal locking and other microphysical mechanisms.

Further compounding the complexity of this response, these materials typically contain macroscopic inhomogeneities such as natural flaws, cracks, joint sets, and bedding planes. The existence of macro-structural heterogeneities in geo-systems renders them vulnerable to catastrophic failures at drastically lower loads than those expected for intact structures. Brittle faulting can be triggered from these zones and propagate under crack opening (mode I), sliding (mode II) or a mixture of modes. Notably, in gravity dams most of the observed cracks are mixed mode (Kishen and Singh (2001); Roth et al. (2015)), and hydraulic fractures propagate in mixed-mode conditions from the walls of wellbores (Rahman et al. (2002)).

Over the past decades, multiple laboratory tests with different configurations (including circular disc (Al-Shayea (2005); Erarslan and Williams (2012)), semi-circular disc(Aliha et al. (2010); Aliha and Ayatollahi (2013)), round bar, and rectangular-beam (Rinehart et al. (2015))) have been designed to investigate the mixed-mode fracture behavior in geomaterials. Among these tests is the cracked Brazilian disc (CBD) specimen, which has been frequently utilized for rock materials due to the amenity of test specimen preparation from the rock cores. Other reasons in adopting the CBD specimen include the relatively straightforward test procedure with regard to the application of compressive rather than tensile load and the capability to easily replicate various combinations of mode I and II fracture propagation by varying the initial crack inclination angle relative to the applied load.

For many applications, mixed-mode fracture in rocks has been simplified to empirical approaches (Yao (2012); Jaeger et al. (2009)) or linear elastic fracture mechanics (LEFM). In these approaches conventional fracture theories (such as the maximum tangential stress criterion (MTS) (Erdogan and Sih (1963)), the minimum strain energy density criterion Sih (1974), the maximum energy release rate criterion (Hussain et al. (1974))) have been used to predict resistance to and direction of the fracture growth. However, LEFM is not always applicable to geomaterials (see, e.g Rubin (1993)), and other more advanced methods are often computationally challenging to implement.

In the case of quasi-brittle materials, cohesive zone models, which may be traced to the pioneering work of Dugdale (1960) and Barenblatt (1962), are an appropriate alternatives to describe the micromechanical features underlying the evolution of damage in the FPZ. These models interpret the FPZ as an interface along which the displacement jump is related to transferring cohesive tractions. Cohesive zone models have been proposed in various settings (see Park and Paulino (2013) for a review of models), but the best known are the potential-based laws by Tvergaard (1990) and Xu and Needleman (1993) and the linear laws by Camacho and Ortiz (1996) and Ortiz and Pandolfi (1999).

The numerical simulation of crack growth within the finite element method may be carried out with different techniques. One early approach is discrete-crack model employing interface elements so that the crack is allowed to propagate along the boundaries of the finite elements. Though several attempts have been made in a case of crack paths unknown a priori to generate robust and reliable tools for automatic remeshing procedure (see, for example, Maligno et al. (2010); Boussetta et al. (2006)), discrete-crack models still suffer from some shortcomings, such as spurious stress transferring across crack surfaces and mesh bias. To alleviate these numerical difficulties, fine meshes are needed, which lead to large-scale and in computationally expensive systems.

In recent years, models with cracks embedded in finite elements including either nodal enrichment, the eXtended or Generalized finite element method (XFEM or GFEM) (Gupta et al. (2015); Wu et al. (2015); Shen and Lew (2014); Kramer et al. (2013); Chen et al. (2012); Belytschko et al. (2001)), or elemental enrichment, the Embedded finite element method (EFEM) (Weed et al. (2015); Zhang et al. (2015); Linder and Zhang (2014); Wu (2011); Foster et al. (2007); Borja and Regueiro (2001); Armero and Garikipati (1996); Simo et al. (1993)) have been applied successfully to simulation of fracture propagation. A comparative study by Oliver et al. (2006b) showed that EFEM is computationally more efficient than XFEM, though it cannot accurately capture the crack tip stresses. In addition, by focusing on slip patterns, Borja (2008) has elucidated that the extended FE solutions require higher-order crack tip enhancement in order to fully capture the strain singularity at the crack tip and EFEM could predict larger slip (i.e., softer response) compared to the XFEM solutions otherwise. Due to some of the appealing features of the EFEM, computational efficiency being a primary one, we have chosen to adopt this method for the simulation of mixed-mode fracture in CBDs.

The remainder of this paper is organized as follows: Section 2 reviews a recently modified cap plasticity model for geomaterials. In Section 3 first, the kinematics of a strong discontinuity are outlined. Second, to capture the fracture initiation and its orientation, bifurcation theory is reviewed. At the end of Section 3, a cohesive fracture model is summarized to describe evolution of the damage with either coupled opening/sliding displacements or solely frictional slip mode. In Section 4, the finite element approximation using assumed enhanced strain (AES) method is briefly discussed. The numerical implementation of the models for both strain hardening and softening responses is given in Section 5. In Section 6, the numerical efficiency and robustness of both constitutive model and post-localization model are briefly discussed. Finally, Section 7 describes a benchmark example of a CBD specimen to investigate the mixed mode fracture behavior of pre-cracked limestone rock, and the finite element solutions are compared with experimental results.

2. Three-invariant isotropic kinematic hardening cap plasticity model

Even though recently various multiscale computational approaches (see for example Tonge and Ramesh (2016); Flores et al. (2015); Oliver et al. (2015); Liu et al. (2015); Cusatis et al. (2014)) have been developed, investigating some micromechanical features of complex geomaterials, continuum plastic constitutive models are still the most widely acknowledged method to capture material nonlinearities and inelastic behaviors.

Cap plasticity models typically utilized in the modeling of complex mechanical behavior of porous geomaterials capture shear yielding at low mean stress and inelastic compaction at higher mean stress. These models can take into account one or more other aspects such as pressure-sensitive yielding, differences in strength in triaxial compression and extension, dilatancy and the Baushinger effect, among others. In this section, the formulation and numerical implementation of a nonassociated, three-invariant, isotropic and kinematic hardening cap plasticity model are briefly described. The model comprises a pressure-dependent shear yield surface, hardening compaction cap and newly added elliptical tension cap as shown in Fig. 1. For more details and motivation of the model, the reader is referred to Motamedi and

Foster (2015).

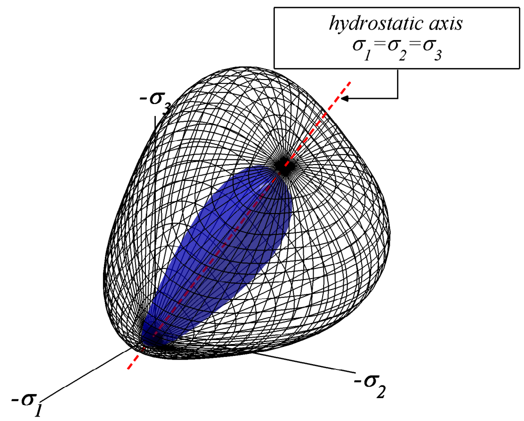

Figure 1: Cap plasticity model: three dimensional view of the yield surface (the exterior free mesh surface) and plastic potential surface (the interior blue solid) in principal stress space.

2.1. Yield functions and plastic potentials

Assuming that the yielding behavior is isotropic, the yield function f and plastic potential function g can be expressed in terms of stress invariants (e.g. I_1, J_2 and J_3). In the case of kinematic hardening, a deviatoric backstress tensor $\boldsymbol{\alpha}$ is presented to capture the Bauschinger effect, such that the relative stress tensor can be defined as $\boldsymbol{\xi} = \boldsymbol{\sigma} - \boldsymbol{\alpha}$. Given a back stress with an appropriate translation rule (Foster et al. (2005)), the yielding of the material may be expressed in terms of invariants of the relative stress (I_1, J_2^{ξ} and J_3^{ξ}).

Many cap plasticity models have been proposed, for example Lu and Fall (2015); Gamnitzer and Hofstetter (2015); DorMohammadi and Khoei (2008); Kohler and Hofstetter (2008); Grueschow and Rudnicki (2005). In this work, we follow a smooth cap formulation initially proposed by Fossum and Brannon (2004). The yield function f and conjugated plastic potential g take the following form:

$$f = \Gamma(\beta^{\xi})\sqrt{J_2^{\xi}} - \sqrt{F_c}(F_f - N) \tag{2.1}$$

$$g = \Gamma(\beta^{\xi})\sqrt{J_2^{\xi}} - \sqrt{F_c^g}(F_f^g - N) \tag{2.2}$$

where the material parameter N indicates the maximum allowed translation of the initial yield surface during kinematic hardening and Γ accounts for the difference in triaxial extension vs. compression strength. The Lode angle β^{ξ} is the function of second and third invariants of the deviatoric relative stress $\mathrm{dev}\xi$. The exponential shear failure function F_f and the corresponding plastic potential surface F_f^g are given as

$$F_f(I_1) = A - C\exp(B\, I_1) - \theta I_1 \tag{2.3}$$

$$F_f^g(I_1) = A - C\exp(L\, I_1) - \phi I_1 \tag{2.4}$$

The shear failure surface F_f captures the pressure dependence of the shear strength of the material where A, B, C and θ are all non-negative material parameters determined from peak stress experimental data, using a procedure described in (Fossum and Brannon (2004)). L and ϕ are determined from experimental measurements of volumetric plastic deformation. The cap function F_c generates two smooth elliptical caps to the yield function in both tensile and compressive stress zones. This function couples hydrostatic and deviatoric stress-induced deformation of the material. The cap function F_c and the corresponding one for plastic potential F_c^g are formulated as

$$F_c(I_1, \kappa) = 1 - H(\kappa - I_1)\left(\frac{I_1 - \kappa}{X(\kappa) - \kappa}\right)^2 - H(I_1 - I_1^T)\left(\frac{I_1 - I_1^T}{3T - I_1^T}\right)^2 \quad (2.5)$$

$$F_c^g(I_1, \kappa) = 1 - H(\kappa - I_1)\left(\frac{I_1 - \kappa}{X^g(\kappa) - \kappa}\right)^2 - H(I_1 - I_1^T)\left(\frac{I_1 - I_1^T}{3T - I_1^T}\right)^2 \quad (2.6)$$

where κ stands for the branch point in which combined porous/microcracked yield surface deviates from the nonporous profile for full dense bodies. The function $X(\kappa)$ is the intersection of the cap surface with the I_1 axis in the $\sqrt{J_2}$ versus I_1 plane and signifies the position at which pressure under pure hydrostatic loading would be sufficient to prompt grain crushing and pore collapse mechanisms.

Furthermore, this plasticity model is furnished with two internal variables, $\boldsymbol{\alpha}$ and κ. The translational back stress tensor $\boldsymbol{\alpha}$ is adopted to capture kinematic hardening. Additionally, on the cap surface, κ is a scalar isotropic hardening parameter, which allows the yield surface to isotropically expand. The combined isotropic/kinematic hardening of the cap model is visualized by the schematic diagram in Fig. 3. The description of evolution laws for

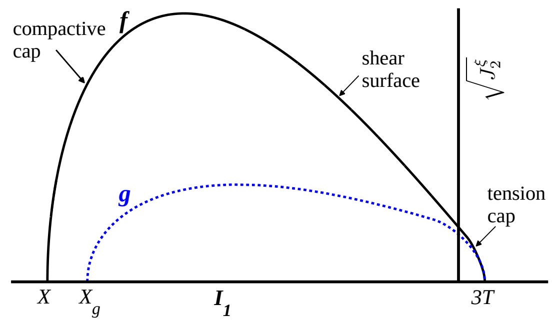

Figure 2: Two-dimensional representation of yield and potential surfaces in meridional stress space; deviatoric stress $\sqrt{J_2}$ versus mean stress I_1.

isotropic/kinematic hardening parameters and their correspondence with microstructural deformations are discussed in Motamedi and Foster (2015).

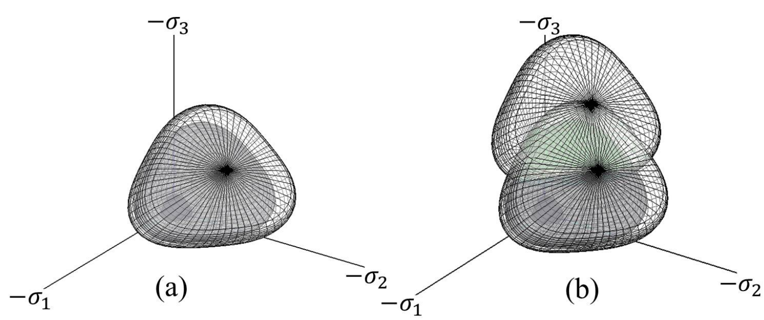

Figure 3: Three dimensional view of initial yield surface (the interior gray solid) evolution in principal stress space for: (a) isotropic hardening and (b) mixed isotropic-kinematic hardening.

2.2. Generalized Hooke's law and flow rule

The generalized Hooke's law for linear isotropic elasticity can be written as:

$$\dot{\boldsymbol{\sigma}} = \boldsymbol{C}^e : \dot{\boldsymbol{\epsilon}};\ \boldsymbol{C}^e = \lambda \mathbf{1} \otimes \mathbf{1} + 2\mu \boldsymbol{I} \tag{2.7}$$

where $\mathbf{1}$ is the second order identity tensor, $\boldsymbol{I}$ is the fourth-order symmetric identity tensor, λ and μ are the Lamé parameters and $\boldsymbol{C}^e$ is the fourth-order isotropic elasticity tensor. For infinitesimal strain, an additive decomposition of the total strain rate $\dot{\boldsymbol{\epsilon}}$ into the elastic and plastic parts is introduced

$$\dot{\boldsymbol{\epsilon}} = \dot{\boldsymbol{\epsilon}}^e + \dot{\boldsymbol{\epsilon}}^p \tag{2.8}$$

A non-associative flow rule is assumed for plastic flow as below

$$\dot{\boldsymbol{\epsilon}}^p = \dot{\gamma}\frac{\partial g}{\partial \boldsymbol{\sigma}} \tag{2.9}$$

In addition, the continuum elasto-plastic tangent $\boldsymbol{C}^{ep}$ can be derived as the following

$$\dot{\boldsymbol{\sigma}} = \boldsymbol{C}^{ep} : \dot{\boldsymbol{\epsilon}};\ \boldsymbol{C}^{ep} = \left(\boldsymbol{C}^e - \frac{1}{\chi}\boldsymbol{C}^e : \frac{\partial g}{\partial \boldsymbol{\sigma}} \otimes \frac{\partial f}{\partial \boldsymbol{\sigma}} : \boldsymbol{C}^e\right) \tag{2.10}$$

in which

$$\chi = \frac{\partial f}{\partial \boldsymbol{\sigma}} : \boldsymbol{C}^e : \frac{\partial g}{\partial \boldsymbol{\sigma}} - \frac{\partial f}{\partial \boldsymbol{\alpha}} : \boldsymbol{h}^{\boldsymbol{\alpha}} - \frac{\partial f}{\partial \kappa} h^{\kappa} \tag{2.11}$$

3. Strong discontinuity:

3.1. Kinematics and governing equations

For strong discontinuities, the displacement field experiences a spatial jump $[\![\boldsymbol{u}]\!] = \boldsymbol{u}^+ - \boldsymbol{u}^-$ across the material surface S separating the subdomains Ω^- and Ω^+ of an otherwise continuous body Ω, see Fig. 4. The displacement field in the context of strong discontinuity kinematics is given by

$$\boldsymbol{u}\left(\boldsymbol{x},t\right) := \underbrace{\bar{\boldsymbol{u}}\left(\boldsymbol{x},t\right)}_{continuious\ part} + \underbrace{[\![\boldsymbol{u}(t)]\!]\, H_S\left(\boldsymbol{x}\right)}_{jump\ discontinuity} \tag{3.1}$$

in which $H_S\left(\boldsymbol{x}\right)$ is the Heaviside function across the surface defined by the conditions

$$H_S\left(\boldsymbol{x}\right) = \begin{cases} 1 \quad \texttt{if} \quad \boldsymbol{x} \in \Omega^+ \\ 0 \quad \texttt{if} \quad \boldsymbol{x} \in \Omega^- \end{cases} \tag{3.2}$$

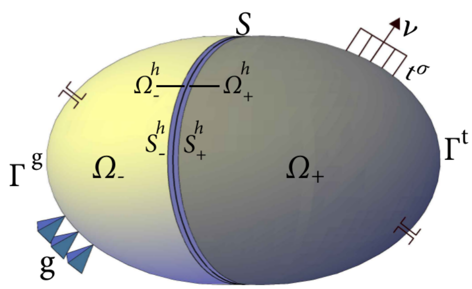

Figure 4: Body Ω with planar strong discontinuity S fixed at the reference configuration, (Ω=$\Omega^+ \cup \Omega^- \cup S$, Γ= $\Gamma^t \cup \Gamma^g$)

.

In this study, it is assumed that the jump discontinuity $[\![\boldsymbol{u}]\!]$ is piecewise constant along surface S (i.e. independent of x) so that the gradient $\boldsymbol{\nabla}\, [\![\boldsymbol{u}]\!]$ is ignored. The total strain rate tensor resulting from this field is the symmetric component of the displacement gradient tensor, which can be derived in compact form as below

$$\dot{\boldsymbol{\epsilon}} := \underbrace{\mathrm{sym}(\nabla \dot{\bar{\boldsymbol{u}}})}_{regular\ part} + \underbrace{\mathrm{sym}\left([\![\dot{\boldsymbol{u}}]\!] \otimes \boldsymbol{n} \right) \delta_S}_{singular\ part} \tag{3.3}$$

where $\boldsymbol{n}$ is the unit normal vector to the surface S and pointing in the direction of Ω^+. The Dirac delta distribution δ_s indicates unbounded strain at the discontinuity interface.

The local form of quasi-static, isothermal equilibrium for a body with strong discontinuity leads to the following set of governing equations

$$\nabla \cdot \boldsymbol{\sigma} + \boldsymbol{b} = \boldsymbol{0} \ \texttt{in} \ \Omega \tag{3.4a}$$

$$\boldsymbol{\sigma} \cdot \boldsymbol{\nu} = \boldsymbol{t}^{\sigma} \ \texttt{on} \ \Gamma^t \tag{3.4b}$$

$$\boldsymbol{u} = \boldsymbol{g} \ \texttt{on} \ \Gamma^g \tag{3.4c}$$

$$[\![\boldsymbol{\sigma}]\!] \cdot \boldsymbol{n} = \boldsymbol{0} \ \texttt{across} \ S \tag{3.4d}$$

where $\boldsymbol{\sigma}$ is the Cauchy stress tensor, $\boldsymbol{b}$ the body force vector, $\boldsymbol{\nu}$ the outward unit normal vector to Γ^t, $\boldsymbol{t}^{\sigma}$ the traction on Γ^t, $\boldsymbol{g}$ the prescribed displacement on Γ^g, and $[\![\boldsymbol{\sigma}]\!]$ is the jump in stress across S.

3.2. Onset of localization: bifurcation analysis

In the material failure mechanics, there exist different approaches to investigate the onset of localized deformation in terms of macrocracks and/or deformation bands. Among them we can point out the local path-independent criterion (Haghighat and Pietruszczak (2015)), bifurcation analysis (Tjioe and Borja (2016); Borja et al. (2013); Regueiro and Foster (2011)), critical plane framework (Pietruszczak and Mroz (2001)). For inelastic materials such as those considered here, linear elastic fracture theory cannot be used. Nonlinear theories, such as the J-Integral, have been applied within the eXtended Finite Element Method (e.g Duflot (2007); Mohammadi (2008)). This theory, however, requires path integration through several elements and adapting the integration points to calculate the integral, and may not be path independent for complex plasticity models that may experience unloading. Bifurcation theory, in contrast, depends solely on the local tangent modulus in the small strain case, and hence is often used in conjunction with plasticity and damage models.

In this section, the localization condition is derived in terms of bifurcation analysis in conjunction with the cap plasticity model proposed earlier in Section 2. This theory is originated at first by the work of Hill (1962) to explore the onset of inelastic behavior in solids using the physics of wave propagation through the matter. Later on Rudnicki and Rice (1975) adopted this work to develop mathematical framework for detecting shear band localization in solids. It has been shown (Regueiro and Foster (2011); Rice and Rudnicki (1980)) that continuous bifurcation precedes discontinuous case. For continuous bifurcation, the plastic loading appears outside and within the discontinuity band at the instant of localization. Thus for strong discontinuities the plastic consistency parameter reads:

$$\dot{\gamma} = \dot{\bar{\gamma}} + \dot{\gamma}_\delta \delta_S \tag{3.5}$$

Similarly, in order for the stress-like internal state variables (ISVs), including the backstress $\boldsymbol{\alpha}$ and the isotropic hardening parameter κ, to be bounded (and the plastic dissipation to be well-defined, the hardening moduli c^α and c^κ have distributional forms (Simo et al. (1993); Regueiro and Foster (2011))

$$\begin{aligned}
(c^\alpha)^{-1} &= (\bar{c}^\alpha)^{-1} + (c^\alpha_\delta)^{-1}\delta_S \\
(c^\alpha)^{-1}\dot{\boldsymbol{\alpha}} &= \dot{\gamma} G^\alpha \operatorname{dev}\left(\frac{\partial g}{\partial \boldsymbol{\sigma}}\right) \\
\dot{\boldsymbol{\alpha}} &= \bar{c}^\alpha G^\alpha \dot{\bar{\gamma}} \operatorname{dev}\left(\frac{\partial g}{\partial \boldsymbol{\sigma}}\right) = \bar{\boldsymbol{h}}^\alpha \dot{\bar{\gamma}} \\
\dot{\boldsymbol{\alpha}} &= c^\alpha_\delta G^\alpha \dot{\gamma}_\delta \operatorname{dev}\left(\frac{\partial g}{\partial \boldsymbol{\sigma}}\right) = \boldsymbol{h}^\alpha_\delta \dot{\gamma}_\delta
\end{aligned} \tag{3.6}$$

$$\begin{aligned}
(c^\kappa)^{-1} &= (\bar{c}^\kappa)^{-1} + (c^\kappa_\delta)^{-1}\delta_S \\
(c^\kappa)^{-1}\dot{\kappa} &= \dot{\gamma} G^\kappa \, tr\left(\frac{\partial g}{\partial \boldsymbol{\sigma}}\right) \\
\dot{\kappa} &= \bar{c}^\kappa G^\kappa \dot{\bar{\gamma}} \, tr\left(\frac{\partial g}{\partial \boldsymbol{\sigma}}\right) = \bar{h}^\kappa \dot{\bar{\gamma}} \\
\dot{\kappa} &= c^\kappa_\delta G^\kappa \dot{\gamma}_\delta \, tr\left(\frac{\partial g}{\partial \boldsymbol{\sigma}}\right) = h^\kappa_\delta \dot{\gamma}_\delta
\end{aligned} \tag{3.7}$$

Substitution of Eqs.(3.5), (3.6) and (3.7) in consistency condition, and solving for both regular and singular parts of the consistency condition gives

$$\dot{\bar{\gamma}} = \frac{1}{\bar{\chi}} \frac{\partial f}{\partial \boldsymbol{\sigma}} : \boldsymbol{C}^e : \dot{\boldsymbol{\epsilon}}^0 \tag{3.8a}$$

$$\bar{\chi} = \frac{\partial f}{\partial \boldsymbol{\sigma}} : \boldsymbol{C}^e : \frac{\partial g}{\partial \boldsymbol{\sigma}} - \frac{\partial f}{\partial \boldsymbol{\alpha}} : \bar{\boldsymbol{h}}^{\alpha} - \frac{\partial f}{\partial \kappa} \bar{h}^{\kappa}$$

$$\dot{\gamma}_\delta = \frac{\frac{\partial f}{\partial \boldsymbol{\sigma}} : \boldsymbol{C}^e : \mathrm{sym}(\llbracket \dot{\boldsymbol{u}} \rrbracket \otimes \boldsymbol{n})}{\frac{\partial f}{\partial \boldsymbol{\sigma}} : \boldsymbol{C}^e : \frac{\partial g}{\partial \boldsymbol{\sigma}}} \tag{3.8b}$$

In addition, we can write the stress rate on the discontinuity surface $\dot{\boldsymbol{\sigma}}^1$ and outside that surface $\dot{\boldsymbol{\sigma}}^0$ as below

$$\begin{aligned} \dot{\boldsymbol{\sigma}}^1 = & \underbrace{\left(\boldsymbol{C}^e - \frac{1}{\chi} \boldsymbol{C}^e : \frac{\partial g}{\partial \boldsymbol{\sigma}} \otimes \frac{\partial f}{\partial \boldsymbol{\sigma}} : \boldsymbol{C}^e \right)}_{\bar{\boldsymbol{C}}^{ep}} : \dot{\boldsymbol{\epsilon}}^0 + \\ & \underbrace{\left(\boldsymbol{C}^{ep} - \frac{\boldsymbol{C}^e : \frac{\partial g}{\partial \boldsymbol{\sigma}} \otimes \frac{\partial f}{\partial \boldsymbol{\sigma}} : \boldsymbol{C}^e}{\frac{\partial f}{\partial \boldsymbol{\sigma}} : \boldsymbol{C}^e : \frac{\partial g}{\partial \boldsymbol{\sigma}}} \right)}_{\tilde{\boldsymbol{C}}^{ep}} : \mathrm{sym}\left(\llbracket \dot{\boldsymbol{u}} \rrbracket \otimes \boldsymbol{n} \right) \delta_S \end{aligned} \tag{3.9a}$$

$$\dot{\boldsymbol{\sigma}}^0 = \bar{\boldsymbol{C}}^{ep} : \dot{\boldsymbol{\epsilon}}^0 \tag{3.9b}$$

where $\tilde{\boldsymbol{C}}^{ep}$ is recognized as the elastic-perfectly plastic tangent modulus.

On the basis of Eq. (3.4d), imposing the traction continuity across the discontinuity surface ($\dot{\boldsymbol{\sigma}}^1 \cdot \boldsymbol{n} = \dot{\boldsymbol{\sigma}}^0 \cdot \boldsymbol{n}$) constitutes the classical condition on the localization tensor $\tilde{\boldsymbol{A}}$ already identified in Regueiro and Foster (2011).

$$\underbrace{(\boldsymbol{n} \cdot \tilde{\boldsymbol{C}}^{ep} \cdot \boldsymbol{n})}_{\tilde{\boldsymbol{A}}} [\![\dot{\boldsymbol{u}}]\!] \, \delta_S = 0$$
$$\Rightarrow \ \det \tilde{\boldsymbol{A}} = 0 \ \text{ for } \ [\![\dot{\boldsymbol{u}}]\!] \neq \underline{0} \tag{3.10}$$

in which $\boldsymbol{n}$ indicates the most critical orientation of the discontinuity surface in the localized element. The above equation states that a nontrivial solution for the traction continuity condition is, of course, possible only when $\tilde{\boldsymbol{A}}$ is singular.

For discontinuous bifurcation, we assume that the plastic loading is localized to the discontinuity band ($\boldsymbol{x} \in S$), whereas the material points immediately adjacent to the band transfer into an elastic unloading state. As a result, the consistency parameter takes the form of

$$\dot{\gamma} = \dot{\gamma}_\delta \delta_S \tag{3.11}$$

Similarly, the hardening moduli would bifurcate in order to have well-defined plastic dissipation.

$$(c^\alpha)^{-1} = (c^\alpha_\delta)^{-1} \delta_S \text{ and } (c^\kappa)^{-1} = (c^\kappa_\delta)^{-1} \delta_S \tag{3.12}$$

Furthermore, by imposing traction continuity requirement, again we can arrive at the localization condition manifested in Eq.(3.10). Following the

Foster et al. (2007), we use a numerical algorithm to solve $\det\tilde{\boldsymbol{A}} = 0$ for the band normal $\boldsymbol{n}$ and then $\tilde{\boldsymbol{A}}\,[\![\dot{\boldsymbol{u}}]\!] = \boldsymbol{0}$ for the deformation directions at the inception of localization.

3.3. Evolution of the displacement jump: post-localization model

In this section, a post-localization model is introduced to describe the softening response of the material after localization detection. In particular, a novel cohesive traction-separation law recently presented in Weed et al. (2015) is utilized to characterize the macro-crack evolution in terms of the displacement jump on the slip surface S. Therefore, similar to the concept of cohesive zone models for quasi-brittle materials (see Camacho and Ortiz (1996); Carol et al. (1997); Sancho et al. (2006); de Borst et al. (2006)), a damage-like function F is proposed in two forms of the tensile and compressive regime as below:

$$F_{\text{tension}} = \underbrace{\sqrt{(\tau_s)^2 + (\alpha_\sigma \langle \sigma_n \rangle)^2}}_{\sigma_{\text{eq}}} - c_{\text{eq}} \tag{3.13a}$$

$$F_{\text{compression}} = |\tau_s - c_{\text{eq}} \cdot \text{sign}(\zeta_s)| - \langle -\sigma_n \rangle \tan\phi' \tag{3.13b}$$

where the normal traction σ_n and tangential traction τ_s attribute to the slip surface. The notation $\langle \bullet \rangle$ represents the Macaulay brackets, taking into account the positive portion, α_σ is a normal stress weighting factor and ϕ' is the friction angle on the slip surface. In addition, the non-negative parameters σ_{eq} and c_{eq} indicate the equivalent traction and equivalent cohesive strength of the band, respectively. Notably, the term sign(ζ_s) devised in Eq. 3.13b would imply that the cohesion on the slip surface operates as a restoring force, i.e. the force c_{eq} always acts in the opposite direction of the displacement jump (or separation) vector. The initial cohesion c_0 is computed in a manner to be balanced with the bulk stress state at the moment of localization.

In the literature, various softening relations have been proposed for a wide range of materials, such as trapezoidal function for a high-strength-low-alloy (HSLA) steel (Scheider and Brocks (2003)); exponential function for a C-300 steel (Ortiz and Pandolfi (1999)); linear softening function for a polycrystalline brittle materials (Espinosa and Zavattieri (2003); Benedetti and Aliabadi (2013)); and linear, bilinear, and exponential softening functions for concrete (Galvez et al. (2002); Bazant (2002)). Here, however, a linear softening curve is adopted for the sake of simplicity. Furthermore, for rock materials like limestone, a linear model has been found to be adequate (Rinehart et al. (2015)). Therefore as depicted in Fig. 5, for the tensile regime the elliptical damage surface $F = 0$ shrinks to the origin while c_{eq} decreases linearly toward zero as the equivalent displacement jump increases.

$$c_{\text{eq}} = c_0 \left(1 - \frac{\zeta_{max}}{\zeta_c}\right) \tag{3.14}$$

where ζ_c denotes to the characteristic slip (or separation) distance, beyond which complete failure occurs in the sense that the crack surface entirely loses its cohesive strength. The scalar ζ_{eq} indicates the equivalent jump magnitude and takes the form of

$$\zeta_{\text{eq}} = \sqrt{\zeta_s^2 + (\alpha_\zeta \zeta_n)^2} \tag{3.15}$$

in which the variables ζ_n and ζ_s are normal opening and tangential (in-plane sliding) slip on the localization band. The parameter α_ζ is a coefficient weighing the relative contribution of the opening and sliding modes in the damage process. Following the spirit of damage mechanics in the unloading/reloading case, we assume c_{eq} unloads elastically to the origin. Likewise, the reloading path is also considered elastic until the point of maximum equivalent separation ζ_{max} attained up until the current time. Beyond this point the softening process will resume. The slope of the unloading-reloading curve can be thought of as the stiffness of the cohesion force and derived as

$$k_c = \frac{c}{\zeta_{max}} = c_0 \left(\frac{1}{\zeta_{max}} - \frac{1}{\zeta_c} \right) \tag{3.16}$$

Subsequently, the equivalent stress on the band can be rewritten as (Weed et al. (2015))

$$\sigma_{\text{eq}} = k_c \, \zeta_{\text{eq}} \tag{3.17}$$

In a number of previous studies, (for example Borja et al. (2013); Foster et al. (2007); Chen et al. (2011)), only one degree of freedom is incorporated into the model which represents sliding displacement with a jump dilation angle ψ' with respect to the discontinuity surface for non-associated plasticity models. It should be remarked that the single sliding degree of freedom may cause spurious hardening and/or a geometric locking effect during non-smooth crack propagation. Particularly, in the mixed mode fracture where crack kinking phenomena are frequently observed, using the one-dimensional separation law could trigger slippage impedance in the deformation band, ultimately resulting in significant convergence problem for numerical implementation. The model proposed in this study tackles this issue allowing the crack surfaces to separate in a coupled opening and sliding mode in the tensile regime.

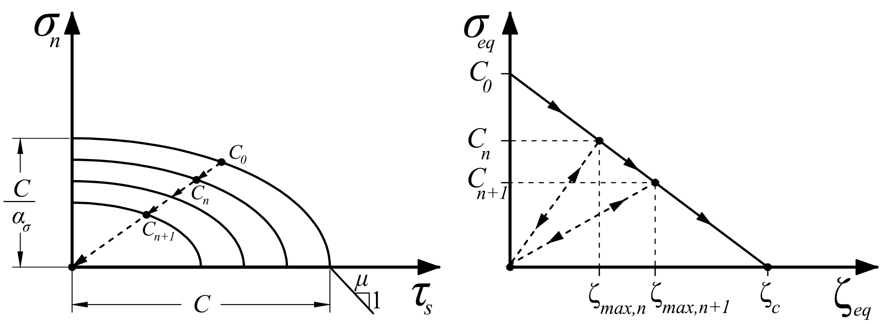

Figure 5: Cohesive fracture law: (a) isotropic softening of the damage-like surface $F = 0$ in traction (σ_n, τ_s) space (b) equivalent traction-separation relationship with corresponding loading-unloading paths. ζ_{max} indicates the maximum attained equivalent separation.

The specific fracture energy G is the amount of external energy required to form a unit surface area of the fully-separated (or damaged) crack. This softening property can be simply computed from the area under the traction-separation function in Fig. 5b. In view of this fact, we can assign different specific fracture energies to each of the respective failure modes (I and II) by assigning $\alpha_\sigma, \alpha_\zeta \neq 1$.

$$\alpha_\sigma \alpha_\zeta = \frac{G_{II}}{G_I} \tag{3.18}$$

In this work, we will assume $\alpha_\sigma = \alpha_\zeta$, hence

$$\alpha_\sigma = \alpha_\zeta = \left(\frac{G_{II}}{G_I}\right)^{\frac{1}{2}} \tag{3.19}$$

It is worth noting that in the compressive case (i.e., crack closure), the frictional resistance always operates on the crack surface independently of the softening process. Indeed, once the cohesion strength completely degrades ($\zeta_{max} = \zeta_c$), the cohesive crack surface evolves to a Coulomb friction surface with friction coefficient $\mu = \tan\phi'$. In this work, we consider a static coefficient of friction, though to get more realistic results a variable coefficient, as in Borja and Foster (2007); Foster et al. (2007), can be used.

4. Finite element implementation: the AES method

In order to incorporate strong discontinuity analysis into the platform of finite element simulation, the assumed enhanced strain (AES) method based on the Hu-Washizu principle is invoked (Borja (2008); Foster et al. (2007); Simo et al. (1993)). In this approach, the displacement discontinuity is conceptualized as an appropriate incompatible mode and added to the standard FE solutions. Note that the AES method is numerically appealing technique since the enhancements for discontinuities are condensed out locally and hence no additional global degrees of freedom are added to the calculations. In doing so, the standard static condensation algorithm is considered to confine the enhancement within the element level.

Figure 6 demonstrates the underlying idea behind the finite element implementation. As shown, a constant strain triangle (CST) element is traced by a discontinuity surface S^e. In addition, we postulate a piecewise constant interpolation of the displacement jump, i.e. $[\![\boldsymbol{u}]\!] = \zeta \boldsymbol{m}$.

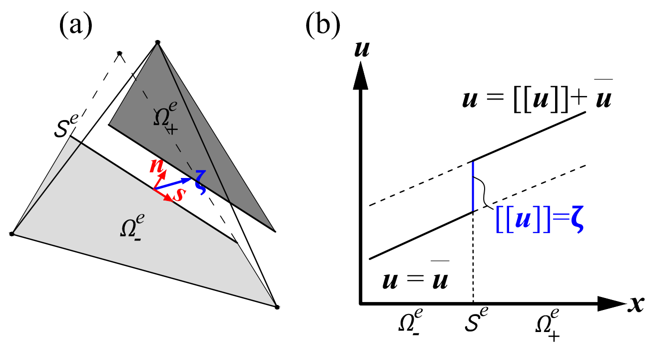

Figure 6: Enhancing a CST finite element: (a) element breaks into two parts (triangle with bold lines represents the conforming deformation.); Vectors $\boldsymbol{n}$ and $\boldsymbol{s}$ indicate the normal and tangential separations across the S^e, respectively. (b) displacement field with a jump across a slip plane.

The strain rate tensor for infinitesimal deformation is written as

$$\dot{\boldsymbol{\epsilon}} = \nabla^s \dot{\boldsymbol{u}} = \underbrace{\nabla^s \dot{\tilde{\boldsymbol{u}}}}_{conforming} + \underbrace{\left(-[\![\dot{\boldsymbol{u}}]\!] \otimes \nabla f^h\right)^s + \left([\![\dot{\boldsymbol{u}}]\!] \otimes \boldsymbol{n}\right)^s \delta_S}_{enhanced} \tag{4.1}$$

which can be regularized in a form of

$$\dot{\boldsymbol{\epsilon}} = \nabla^s \dot{\boldsymbol{u}} = \underbrace{\nabla^s \dot{\tilde{\boldsymbol{u}}} + \left(-[\![\dot{\boldsymbol{u}}]\!] \otimes \nabla f^h\right)^s}_{\dot{\boldsymbol{\epsilon}}^{reg}} + \underbrace{\left([\![\dot{\boldsymbol{u}}]\!] \otimes \boldsymbol{n}\right)^s \delta_S}_{singular} \tag{4.2}$$

The function $f^h(\boldsymbol{x})$ is a smooth blending function for localized elements that may be conveniently defined as the sum of the shape functions attributed to the active nodes.

$$f^h = \sum_{A=1}^{n_{en}} N_A H_S\left(\boldsymbol{x}_A\right) \tag{4.3}$$

where n_{en} is the number of nodes for a localized element, and N_A are the standard finite element shape functions. Using such a kinematic description affords the formulation the ability to allow the essential boundary conditions, Γ^g in Figure 4, to be applied exclusively on the conforming displacement term $\tilde{\boldsymbol{u}}(\boldsymbol{x}, t)$. As a result, the nodal displacements calculated at the global level can be realized as the final displacements. Eventually, the finite element stress for localized elements can be obtained from the regular part of the strain $\dot{\boldsymbol{\epsilon}}^{reg}$. The relevant mathematical background is discussed in Borja and Regueiro (2001). Thus, for elastic unloading we have

$$\dot{\boldsymbol{\sigma}} = \boldsymbol{C}^e : \dot{\boldsymbol{\epsilon}}^{reg} \tag{4.4}$$

For further details of the AES method, including its variational and matrix formulation, the reader is referred to Borja (2008) and the references therein.

5. Numerical implementation

Numerical integration of the constitutive models plays a pivotal role in successfully modeling boundary value problems in engineering. Herein, a well established integration technique called the implicit return mapping algorithm is invoked. This algorithm affords first-order accuracy while satisfying the conditions for unconditional stability.

5.1. Cap plasticity model

To solve the non-linear material model proposed in Section 2, we employ the well-known Newton-Raphson (N-R) iterative method. This method basically constructs the residual vector $\boldsymbol{R}$ as a function of the unknown variables $\boldsymbol{X}$ as below:

$$\boldsymbol{R}(\boldsymbol{X}) = \left\{ \begin{array}{c} \Delta\boldsymbol{\sigma} + \Delta\gamma[\boldsymbol{C}^e] \cdot (\frac{\partial g}{\partial \boldsymbol{\sigma}}) - \boldsymbol{C}^e : \Delta\boldsymbol{\epsilon} \\ \\ \Delta\boldsymbol{\alpha} - \Delta\gamma \boldsymbol{h}^{\boldsymbol{\alpha}}(\boldsymbol{\alpha}) \\ \\ \Delta\kappa - \Delta\gamma h^{\kappa}(\kappa) \\ \\ f(\boldsymbol{\sigma}, \boldsymbol{\alpha}, \kappa) \end{array} \right\} \text{ in which } \boldsymbol{X} = \left\{ \begin{array}{c} \boldsymbol{\sigma} \\ \boldsymbol{\alpha} \\ \kappa \\ \Delta\gamma \end{array} \right\} \tag{5.1}$$

where $[\boldsymbol{C}^e]$ is the linear elastic stiffness matrix in the Voigt form and $\Delta\gamma$ is the discrete consistency parameter. Here $\boldsymbol{\sigma}$ and $\boldsymbol{\alpha}$ are the Voigt form of the Cauchy stress and backstress tensors, respectively. The implicit stress-integration algorithm is summarized in the Appendix Box 1.

5.2. Post-localization model

Regarding the nonlinear formulation proposed for the combined opening-sliding fracture evolution Eq. 3.13a, we use the standard N-R algorithm to solve for displacement jump $\boldsymbol{\zeta} = (\zeta_n, \zeta_s)$ on the band. As a result, the residual vectors can be defined based on traction balances on the band taking the form of:

$$\Phi_1 = \langle \sigma_n \rangle - k_c \zeta_n = 0 \tag{5.2a}$$

$$\Phi_2 = |\tau_s - k_c \zeta_s| - \langle -\sigma_n \rangle \tan\phi' = 0 \tag{5.2b}$$

It is worth it to mention that in the tensile regime, the residual Φ_2 can be reattained as $\tau_s - k_c \zeta_s = 0$. On the other hand, in the compression case, we can solve only the second residual Φ_2 with no need for any iterative methods. Implicit integration of slip values in terms of whether the slip band is newly detected or if the displacement jump evolution has already been activated on the band is presented in the Appendix (Box 2 and Box 3, respectively).

6. Numerical efficiency and robustness

6.1. Cap plasticity model

Particular mathematical treatments can be exploited to improve the efficiency and robustness of the integration procedure. The first remedy is reducing the number of unknowns in the system of nonlinear equations as the cap plasticity model can be as large as 13 (6 for stress components, 5 for kinematic hardening, 1 for isotropic hardening and 1 for consistency parameter). This number can be reduced to 7 using the spectral decomposition method and sometimes to 6 when the priori shear/cap surface determination technique is applied as well.

In addition to this, the consistent tangent modulus $\boldsymbol{C}_{n+1}^{alg} = \partial\boldsymbol{\sigma}_{n+1}/\partial\boldsymbol{\epsilon}_{n+1}$ is computed in order to gain the quadratic rate of convergence within the framework of implicit integration algorithm. To this end, another remedy which can be applied is recasting the residual vectors with a uniform dimensionality. This feature could enhance the robustness and tractability of the Newton-Raphson procedure as improves the conditioning of the local tangent matrix $D\boldsymbol{R}/D\boldsymbol{X}$ and also reduces the number of iterations required to reach the convergent solutions for $\boldsymbol{X}$. For further elaboration of these algorithms the interested reader is referred to Motamedi and Foster (2015) and Foster et al. (2005).

6.2. Post-localization model

6.2.1. Spurious solutions

Since there is no guarantee whether a trial guess for the state of the band (being in tension or compression) stays valid during the integration procedure, the N-R iteration may converge to a spurious solution for slip value(s). To overcome this drawback, once a change in the sign of the normal traction is detected, the slip on the band should be instead calculated using the appropriate formulation with regard to the new state of the band. Owing to this, a standard linear interpolation is utilized to find a new slip value as the starting point of the subsequent N-R.

$$\zeta_s = \zeta_s^i - \sigma_n^i \cdot \left(\frac{\zeta_s^f - \zeta_s^i}{\sigma_n^f - \sigma_n^i} \right) \tag{6.1}$$

where (σ_n^i, ζ_s^i) are the initial normal traction and slip values at the beginning of the N-R iteration, $\left(\sigma_n^f, \zeta_s^f\right)$ are the spurious converged values and ζ_s is the interpolated shear slip value corresponding to the critical point $(\sigma_n, \zeta_n) = (0, 0)$ in which the sign of the normal traction changes.

6.2.2. Impl-Ex integration scheme

In the finite element simulation of materials undergoing strain softening behavior, even if the nonlinear problem is mathematically well posed and features a unique solution, it is well known that the classical implicit approach may suffer from a lack of robustness during a given iterative procedure. As discussed in detail by Oliver et al. (2006a), if material failure propagates through the solids, the tangent constitutive operator $\boldsymbol{C}_{n+1}^{alg}$ progressively loses its positive definite character which is eventually accompanied by the loss of positive definiteness of the global stiffness matrix.

In order to ameliorate the shortcomings of the fully implicit schemes, we apply an implicit/explicit (Impl-Ex) integration technique adopted from Oliver et al. (2006a). Using this semi-implicit algorithm to seek solution at time step t_{n+1}, the slip values $\boldsymbol{\zeta}$ are explicitly approximated based on their implicitly updated values from prior time steps t_n and t_{n-1}.

$$\tilde{\boldsymbol{\zeta}}_{n+1} = \boldsymbol{\zeta}_n + \frac{\Delta t_{n+1}}{\Delta t_n} \left(\boldsymbol{\zeta}_n - \boldsymbol{\zeta}_{n-1} \right) \tag{6.2}$$

The semi-implicit stress is then calculated

$$\tilde{\boldsymbol{\sigma}}_{n+1} = \boldsymbol{\sigma}_n + \boldsymbol{c}^e : \Delta \boldsymbol{\varepsilon}_{n+1}^{\text{conf}} - \boldsymbol{c}^e : \left(\tilde{\boldsymbol{\zeta}}_{n+1} \otimes \nabla f^h \right)^s \tag{6.3}$$

since $\tilde{\boldsymbol{\zeta}}_{n+1}$ is postulated as a predetermined vector, we can easily derive the effective algorithmic operator C_{n+1}^{eff} as below

$$\boldsymbol{C}_{n+1}^{\text{eff}} = \frac{\partial \tilde{\boldsymbol{\sigma}}_{n+1}}{\partial \boldsymbol{\varepsilon}_{n+1}} = \boldsymbol{C}^e \tag{6.4}$$

Hence, for linear elasticity, the tangent modulus is constant. The modification of taking the entire slip vector, rather than the magnitude as used in Oliver et al. (2006a) was proposed in Weed et al. (2015). This approach, at minor cost of accuracy, improved the efficiency of the simulation by creating

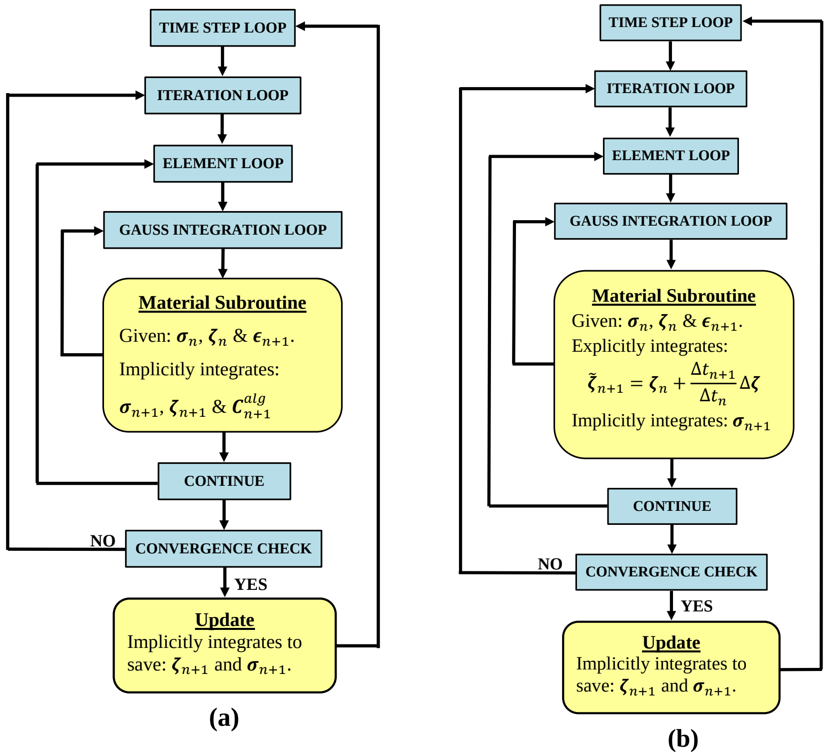

Figure 7: Flowchart for the numerical integration algorithm within a FE code: (a)Implicit scheme, (b)Impl-Ex scheme.

a linear solution in this part. It should be commented that unconditional stability is lost in the system. At the end of the time step, once the convergent solution of the global displacements is obtained, the stress $\boldsymbol{\sigma}$ and slip values $\boldsymbol{\zeta}$ will be implicitly updated to be used as a reference point for the next time step. A flowchart given in Fig. 7 schematically illustrates the difference between the new semi-implicit scheme and the conventional fully implicit algorithm.

7. Numerical benchmark problem:

The cracked Brazilian disc (CBD) test is one of the most acknowledged methods in evaluating mixed-mode fracture behavior of brittle geomaterials. Among the numerous experimental tests that have been conducted in this specimen for different rock materials, we can mention to Keochang granite (Chang et al. (2002)), Yeosan marble (Chang et al. (2002)), Saudi Arabian limestone (Al-Shayea (2005)), Guiting limestone (Aliha et al. (2010)), Dionysos marble (Kourkoulis et al. (2012)), and Neyriz marble (Ayatollahi and Akbardoost (2014)). In this study, the material properties listed in Table 1 were fit to Salem limestone rock by Fossum and Brannon (2004) and frequently reported in Regueiro and Foster (2011), Sun et al. (2013) and Motamedi and Foster (2015). For the specific fracture energy ratio G_{II}/G_I, varied values are calculated experimentally dependent on the specific material of the interest and the fracture test chosen. In this paper, we use the empirical value of $G_{II}/G_I = 4.8$. This value is given in Al-Shayea (2005) for a Saudi Arabian limestone rock tested under the ambient condition using CBD configuration. For the characteristic slip distance ζ_c, the value 0.4 (mm) is assumed (Borja and Foster (2007)).

The generic configuration of the test is illustrated in Fig.(8) and the same as one utilized in the experimental test by Al-Shayea (2005). The circular disk contains a radius R=49mm as well as the crack length ratio $a/R = 0.3$. The angle β stands for orientation of the crack with respect to the loading direction $\boldsymbol{u}$.

Table 1: Material parameters for Salem limestone rock used in the CBD test

Parameter	Value
Young's Modulus (E)	22547 (MPa)
Poisson's Ratio (ν)	0.2524 (dimensionless)
isotropic tensile strength (T)	5 (MPa)
tension cap parameter (I_1^T)	0.0 (MPa)
compression cap parameter (κ_0)	-8.05 (MPa)
shear yield surface parameter (A)	689.2 (MPa)
shear yield surface parameter (B)	3.94e-4 (1/MPa)
shear yield surface parameter (L)	1.0e-4 (1/MPa)
shear yield surface parameter (C)	675.2 (MPa)
shear yield surface parameter (θ, ϕ)	0.0 (rad)
aspect ratios (R, Q)	28.0 (dimensionless)
isotropic hardening parameter (W)	0.08 (dimensionless)
isotropic hardening parameter (D_1)	1.47e-3 (1/MPa)
isotropic hardening parameter (D_2)	0.0 (1/MPa^2)
kinematic hardening parameter (c^α)	1e5 (MPa)
kinematic hardening parameter (N)	6.0 (MPa)
stress triaxiality parameter (ψ)	0.8 (dimensionless)
localized friction angle (ϕ')	40°(degree)
characteristic slip distance (ζ_c)	0.4 (mm)
specific fracture energy ratio (G_{II}/G_I)	4.8 (dimensionless)

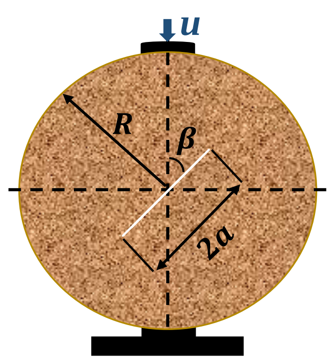

Figure 8: Geometry and loading conditions of CBD specimen subjected to mixed mode I/II loading.

The displacement-controlled loading test is replicated via applying the vertical displacement on the three nodes of top surface of the disk. The three nodes at the bottom surface are fixed in the vertical direction. In order to maintain the global stability of the example, the two nodes located at the crest and trough of the disk are restricted from lateral movement as well. To investigate the effect of mode mixity on crack growth path and failure pattern, the example is performed with three different crack inclination angles ($\beta = 15^{\circ}, 30^{\circ}$, and 55°). In view of the fact that all aforementioned CBD tests captured a clear, continuous fracture surface for rock specimens, we check the localization condition only for tip elements. Hence, the new crack surface will be traced from the crack tip at one edge of the tip element to the opposite edge with the orientation obtained from discontinuous bifurcation analysis described in Section 3.2. This algorithm is visualized schematically in Figure 9. The detection algorithm is only performed at the end of each time step for simplicity. While this introduces some error, it has been shown that the error disappears as the time step is refined Parvaneh and Foster (2016).

To perform the FE simulation, a mesh with 512 CST elements is employed, Figure 10. Deformations are assumed to be infinitesimal. Several theoretical and experimental studies conducted in the past on rock samples with various thicknesses suggest that the specimen thickness has negligible effect on fracture behavior of rock materials (see for example Whittaker et al. (1992) and Khan and Al-Shayea (2000)). As a result, this example is ana-

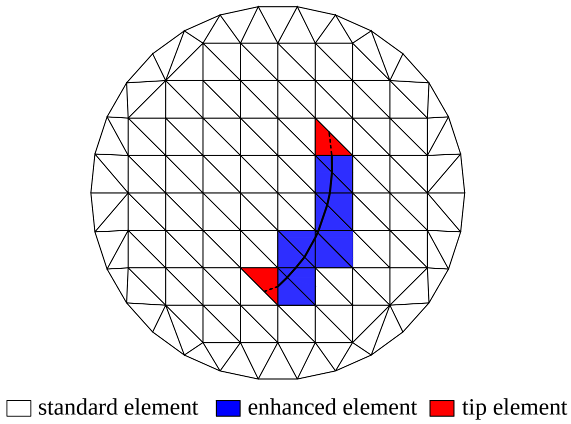

Figure 9: Strategy for tracing the crack propagation path.

lyzed under plane strain condition.

The initial central cracks are introduced in the FE model as a fully damaged part of the specimen using the specific embedded discontinuity surfaces inside the elements as graphically shown in Figure 10. This interface includes zero initial cohesive strength and localized friction angle so that the pre-cracked elements immediately fail when loaded in tension, shear or any of their combinations. These elements can, however, still endure compressive loads.

The paths of crack propagation for three inclination angles are depicted in Figure 10. This plot indicates that the fracture propagation initiates from both ends of the pre-existing cracks, and kinks into a new direction. Subsequently the crack growth continues along a curved path toward the direction of loading. This numerical prediction is quite similar to experimental observations in several laboratory studies, see for example Al-Shayea (2005), Aliha et al. (2010) and Haeri et al. (2014), among others.

The reaction force-versus-downward displacement response is presented in Figure 11. The numerical procedure adequately converges until the end of the curves, to practically null load $\boldsymbol{u}$. For inclination angles β equal to 30 and 55 degrees, there is a convergence issue as the crack approaches the displacement boundaries. As pointed out by Chen et al. (2011) in the AES method, discontinuities which propagate into essential boundary conditions will have difficulty converging. In order to avoid this, they suggest rotating the discontinuity surface slightly so that there is at least one element between the localized elements and the elements which have the assigned boundary conditions. But for β=10 degrees, the entire simulation finishes successfully and a complete softening curve is obtained. Furthermore, the end of the softening curve displays a slight rise in the residual force, which is most likely due to friction effects on the discontinuity surface. There is a noticeable discrepancy between $\beta = 30$ degrees and the two other inclinations angles (10 and 55 degrees) with regard to the maximum reaction force. From the simulation results, the 30 degree angle produces a stress state, within the tip elements, which is more critical for bifurcation analysis than the other two angles. Aliha et al. (2010) carried out different CBD tests for Guiting limestone to investigate the geometry and size effects on fracture trajectory under mixed mode loading. They show that the $\beta = 27$ degrees produces a minimum fracture load, which is in close accord with our simulation results. According to their analytical calculations, derived based on GMTS criterion, this discrepancy could be attributed to the magnitude and sign of the T-stress.

The crack initiation angle θ' is the angle by which the crack extension deviates from the direction of the initial crack inserted inside the specimen. The values of θ' are derived based on bifurcation analysis for tip localized elements and shown in Table 2 . Results are compared with the experimental data provided in Al-Shayea (2005). For lower inclination angles, β=15 and 30 degrees, numerical results accords well with the experiment. But for $\beta = 55^{\circ}$, there is a gap between the results. The main reason for this difference is that the model could not consider the influence of the crack closing which indeed observed in the laboratory tests. However, If the crack initiation angle is recalculated for the first two tip elements, the θ' approaches to the corresponding experimental value. In other words, numerical simulation adjusts its crack path orientation shortly after the slip evolution proceeds in initial cracks.

Table 2: Crack initial angle θ' for CBD test

Inclination angle	$\beta = 15^{\circ}$	$\beta = 30^{\circ}$	$\beta = 55^{\circ}$
Experimental test (Al-Shayea (2005))	26°	70°	81°
Numerical simulation	27°	66°	$58^{\circ}(77.5^{\circ})^{*}$

* The average crack initial angle for the first two tip elements

In the study of the fracture behavior of the disk specimen, additional insights can be gained by comparing the kinematics of deformation. Accordingly, the deformed meshes generated by the AES solution are displayed in Figures 12-14. When the disc is loaded under diametral compression, for lower inclination angles $\beta = 10^{\circ}$ and 30° the two faces of the initial coplanar crack simultaneously open and slide relative to each other. For inclination angle $\beta = 55^{\circ}$, by contrast, the results demonstrated in-plane sliding of the central crack faces. This numerical observation compares with experimental data reported by Al-Shayea (2005) in which a crack extensometer was attached to the pre-existing cracks with a perpendicular position to its orientation. As illustrated by the author, for crack angles of $\beta \leq 45^{\circ}$, the sensor recorded positive values. This observation validates the presence of crack opening deformation at the crack mouth. Conversely, by increasing the crack inclination, the crack closure becomes more pronounced which would be characterized in our model as a pure shear sliding mode. While there is some difference between the saw cut of finite width in the experiment and the crack modeled here, the model is more typical of the type of flaws seen in real geosystems.

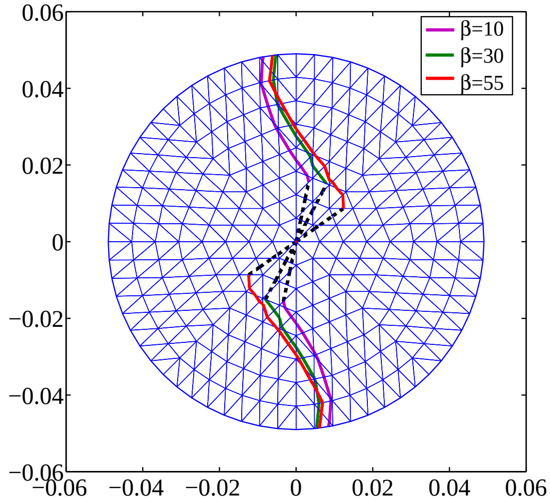

Figure 10: Crack propagation path simulation for CBD specimen with different inclination angle (β=10, 30 and 55). Initial cracks are represented by the dash thick lines through the finite element mesh.

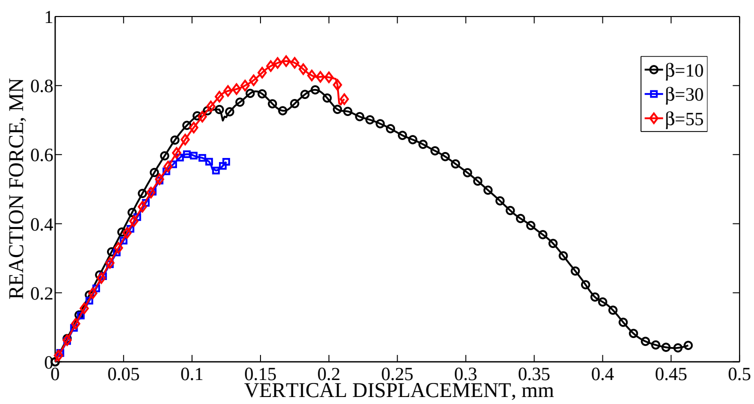

Figure 11: Load-displacement plots for CBD specimen with different inclination angle (β=10, 30 and 55).

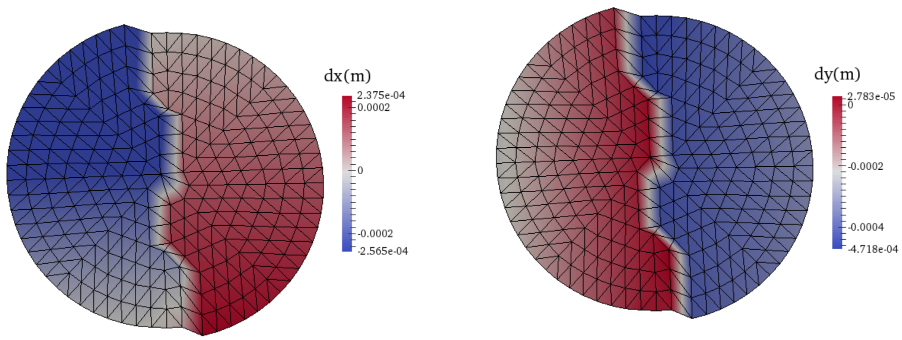

(a) Horizontal displacement contour (b) Vertical displacement contour

Figure 12: Deformed mesh with enhanced solution for inclination angle (β=10).

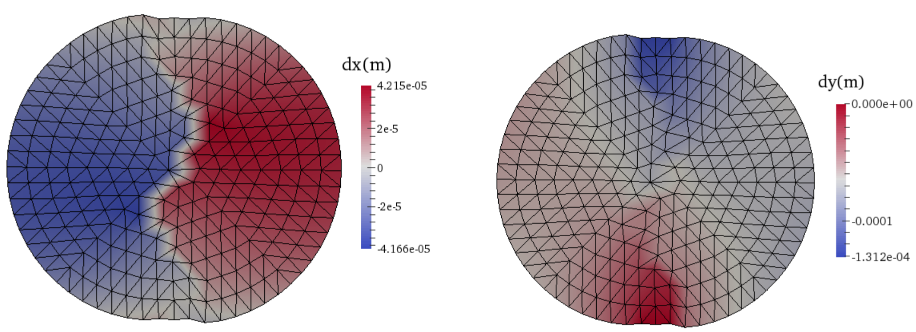

(a) Horizontal displacement contour (b) Vertical displacement contour

Figure 13: Deformed mesh with enhanced solution for inclination angle (β=30).

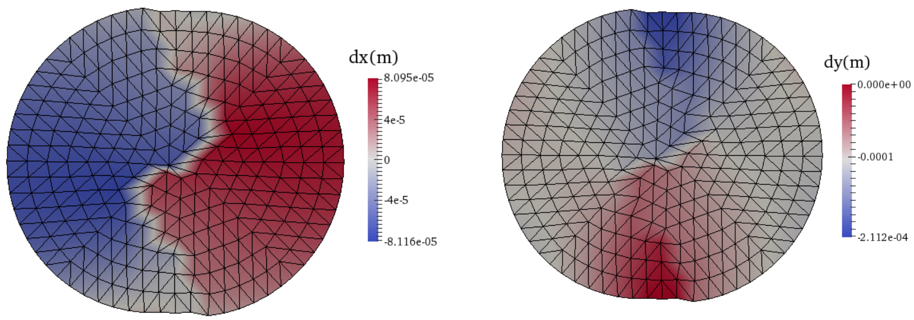

(a) Horizontal displacement contour (b) Vertical displacement contour

Figure 14: Deformed mesh with enhanced solution for inclination angle (β=55).

8. Conclusion

In this paper, a finite element simulation of a mixed-mode fracture propagation for CBD is created. Localized failure is detected by a loss of ellipticity condition, and subsequent post-localization softening is modeled in the framework of an enhanced strain finite element schema. These elements include additional internal degrees of freedom which track both opening and shear displacement on a critically orientated surface determined by bifurcation theory.

Due to the fact that the accuracy of bifurcation prediction is fundamentally dependent on the constitutive model used in the analysis, a three-invariant cap plasticity model based on a non-associated flow rule and combined isotropic/kinematic hardening is adopted. The newly added tension cap to the constitutive model enables us to investigate the inception of dilation bands in addition to shear bands.

To simulate the CBD specimen test, an initial crack is introduced into the model by inserting frictionless interfaces within pre-cracked elements. In addition, assigning a negligible initial cohesion for those cracks leads to the immediate appearance of localized deformations in a form of combined shear/opening fracture. Nevertheless, those pre-localized elements still carry compressive loads as crack closure occurs. The plane strain simulation of the CBD specimen shows good agreement with experimental results contained in the referenced literature. Specifically, the simulation accurately captures the kinking nature of the crack and the overall crack path orientation.

For future work, in order to more precisely replicate load transfer, we consider implementing a contact mechanics formulation to model the interface between the boundary constraints (loading platens in the experiments) and the CBD specimen.

Acknowledgments

The authors would like to acknowledge the support of the National Science Foundation, Grant No. NSF-CMMI 1030398.

Appendix

Here, implicit integration algorithms are provided, demonstrating how stress state and displacement jump values are calculated for cap plasticity model and post-localization model, respectively.

Box 1: implicit stress-point algorithm for cap plasticity model.

Step 1: Compute trial state variables: $\boldsymbol{\sigma}^{tr}_{n+1} = \boldsymbol{\sigma}_n + \boldsymbol{c}^e : \Delta\boldsymbol{\epsilon}_{n+1}$, $\boldsymbol{\alpha}^{tr}_{n+1} = \boldsymbol{\alpha}_n$, $\kappa^{tr}_{n+1} = \kappa_n$.

Step 2: Check the yielding condition: $f^{tr}_{n+1} > 0$?

If no, set $\boldsymbol{\sigma}_{n+1} = \boldsymbol{\sigma}^{tr}_{n+1}$, $\boldsymbol{\alpha}_{n+1} = \boldsymbol{\alpha}_n$, $\kappa_{n+1} = \kappa_n$ and exit.
If yes, Go to step 3

Step 3: Apply particular mathematical treatments to reduce the number of unknowns and hence improve the computational efficiency (see Section 6.1):

Step 4: Initialize $\boldsymbol{X}_0 = \boldsymbol{0}$ and use N-R scheme to solve for converged solution:

$$\delta\boldsymbol{X}^{(k+1)} = [D\boldsymbol{R}/D\boldsymbol{X}]^{-1}\boldsymbol{R}(\boldsymbol{X}^k)$$
$$\boldsymbol{X}^{(k+1)} = \boldsymbol{X}^{(k)} + \delta\boldsymbol{X}^{(k+1)}$$
Until $||\boldsymbol{R}(\boldsymbol{X})||/||\boldsymbol{R}(\boldsymbol{X}_0)|| < \mathrm{tol}_{\boldsymbol{X}}$
where $k+1$ refers to the current iteration.

Step 5: Update state variables $\boldsymbol{\sigma}_{n+1}$, $\boldsymbol{\alpha}_{n+1}$, κ_{n+1} and consistency parameter γ_{n+1} then exit.

Box 2: Implicit algorithm for a newly localized element.

Step 1: Compute trial state variables: $\boldsymbol{\sigma}^{tr}_{n+1} = \boldsymbol{\sigma}_n + \boldsymbol{c}^e : \Delta\boldsymbol{\epsilon}^{reg}$, ${\sigma_n}^{tr}_{n+1} = \boldsymbol{\sigma}^{tr}_{n+1} : (\boldsymbol{n} \otimes \boldsymbol{n})$ and ${\tau_s}^{tr}_{n+1} = \boldsymbol{\sigma}^{tr}_{n+1} : (\boldsymbol{s} \otimes \boldsymbol{n})$.

Step 2: Check for yielding on the band: $F^{tr}_{n+1} > 0$?

If no, band is inactive. Set $\boldsymbol{\sigma}_{n+1} = \boldsymbol{\sigma}^{tr}_{n+1}$ and $\boldsymbol{\zeta}_{n+1} = \mathbf{0}$ then exit.
If yes, band is active. Go to Step 3.

Step 3: Solve for slip values $\boldsymbol{\zeta}_{n+1} = (\zeta_n, \zeta_s)_{n+1}$ on the band:

If $\sigma^{tr}_n > 0$ (tension), If $\boldsymbol{\zeta} = \mathbf{0}$ then initialize $\boldsymbol{\zeta}_0 = tol\,[\sigma_n,\, \tau_s]^T_n$ and use N-R scheme to solve for converged solution:

$$\delta\boldsymbol{\zeta}^{(k+1)} = [D\boldsymbol{\Phi}/D\boldsymbol{\zeta}]^{-1}\boldsymbol{\Phi}(\boldsymbol{\zeta}^k)$$
$$\boldsymbol{\zeta}^{(k+1)} = \boldsymbol{\zeta}^{(k)} + \delta\boldsymbol{\zeta}^{(k+1)}$$
Until $||\boldsymbol{\Phi}(\boldsymbol{\zeta})||/||\boldsymbol{\Phi}(\boldsymbol{\zeta}_0)|| < \mathrm{tol}_{\boldsymbol{\zeta}}$
where $k+1$ refers to the current iteration.

Step 3.1: Check to avoid spurious solution (see Section 6.2.1).

Else $\sigma^{tr}_n < 0$ (crack closure) then solve for ζ_s using 5.2b.

Step 3.2: Check to avoid spurious solution (see Section 6.2.1).

Step 4: Update $\boldsymbol{\zeta}_{n+1}$, $k_{c,n+1}$, and $\boldsymbol{\sigma}_{n+1}$ then exit.

Box 3: Slip algorithm for an element which has pre-existing slip on the band.

Step 1: Compute trial state variables: $\boldsymbol{\sigma}_{n+1}^{tr} = \boldsymbol{\sigma}_n + \boldsymbol{c}^e : \Delta\boldsymbol{\epsilon}^{reg}$, ${\sigma_n}_{n+1}^{tr} = \boldsymbol{\sigma}_{n+1}^{tr} : (\boldsymbol{n} \otimes \boldsymbol{n})$ and ${\tau_s}_{n+1}^{tr} = \boldsymbol{\sigma}_{n+1}^{tr} : (\boldsymbol{s} \otimes \boldsymbol{n})$.

Step 2: Assume elastic unloading/reloading phase on the band,
hence hold k_c as a constant. Set $k_{cn+1} = c_0 \left(\frac{1}{\zeta_{max,n}} - \frac{1}{\zeta_c} \right)$ then:

If $\sigma_n^{tr} > 0$ (tension) solve for slip values $\boldsymbol{\zeta}_{n+1} = (\zeta_n, \zeta_s)_{n+1}$ using the balance equations 5.2a and 5.2b.

Else ($\sigma_n^{tr} < 0$, hence compression)

First, check for slip on the band:

If $|\tau_s - k_c\zeta_s| < \langle -\sigma_n \rangle \tan\phi$

No slip on the band due to frictional lock,
exit with trial stress.

Else

Solve for ζ_s using: 5.2b.

Step 2.1: After slip value(s) calculated, evaluate elastic unloading/reloading assumption: ${\zeta_{eff}}_{n+1} < \zeta_{max,n}$?

If yes, update $\boldsymbol{\sigma}_{n+1}$ and set $\boldsymbol{\zeta}_{max,n+1} = \boldsymbol{\zeta}_{max,n}$ and exit.
If no, the band is in the softening phase,
set k_c as a decreasing variable and use Box 2 to solve for slip value(s).

Step 3: Update $\boldsymbol{\zeta}_{n+1}$, $k_{c,n+1}$ and $\boldsymbol{\sigma}_{n+1}$ then exit.

References

Al-Shayea, N. A., 2005. Crack propagation trajectories for rocks under mixed mode iii fracture. Engineering Geology 81 (1), 84 – 97.
URL http://www.sciencedirect.com/science/article/pii/S0013795205001614

Aliha, M., Ayatollahi, M., 2013. Two-parameter fracture analysis of {SCB} rock specimen under mixed mode loading. Engineering Fracture Mechanics 103 (0), 115 – 123, advances in Failure Assessment Using Fracture and Damage Mechanics.
URL http://www.sciencedirect.com/science/article/pii/S0013794412003839

Aliha, M., Ayatollahi, M., Smith, D., Pavier, M., 2010. Geometry and size effects on fracture trajectory in a limestone rock under mixed mode loading. Engineering Fracture Mechanics 77 (11), 2200 – 2212, international Conference on Crack Paths 2009.
URL http://www.sciencedirect.com/science/article/pii/S0013794410001360

Armero, F., Garikipati, K., 1996. An analysis of strong discontinuities in multiplicative finite strain plasticity and their relation with the numerical simulation of strain localization in solids. International Journal of Solids and Structures 33 (2022), 2863 – 2885.
URL http://www.sciencedirect.com/science/article/pii/002076839500257X

Ayatollahi, M., Akbardoost, J., 2014. Size and geometry effects on rock fracture toughness: Mode i fracture. Rock Mechanics and Rock Engineering 47 (2), 677–687.
URL http://dx.doi.org/10.1007/s00603-013-0430-7

Barenblatt, G., 1962. The mathematical theory of equilibrium cracks in brittle fracture. Advances in Applied Mechanics 7, 55–129.

Bazant, Z. P., 2002. Concrete fracture models: testing and practice. Engineering Fracture Mechanics 69 (2), 165 – 205.
URL http://www.sciencedirect.com/science/article/pii/S0013794401000844

Belytschko, T., Mos, N., Usui, S., Parimi, C., 2001. Arbitrary discontinuities in finite elements. International Journal for Numerical Methods in Engineering 50 (4), 993–1013.
URL http://dx.doi.org/10.1002/1097-0207(20010210)50:4<993::AID-NME164>3.0.CO;2-M

Benedetti, I., Aliabadi, M., 2013. A three-dimensional cohesive-frictional grain-boundary micromechanical model for intergranular degradation and failure in polycrystalline materials. Computer Methods in Applied Mechanics and Engineering 265 (0), 36 – 62.
URL http://www.sciencedirect.com/science/article/pii/S0045782513001503

Borja, R. I., 2008. Assumed enhanced strain and the extended finite element methods: A unification of concepts. Computer Methods in Applied Mechanics and Engineering 197 (3340), 2789 – 2803.
URL http://www.sciencedirect.com/science/article/pii/S0045782508000315

Borja, R. I., Foster, C. D., 2007. Continuum mathematical modeling of slip weakening in geological systems. Journal of Geophysical Research: Solid Earth 112 (B4), 1–12.
URL http://dx.doi.org/10.1029/2005JB004056

Borja, R. I., Regueiro, R. A., 2001. Strain localization in frictional materials exhibiting displacement jumps. Computer Methods in Applied Mechanics and Engineering 190 (2021), 2555 – 2580.
URL http://www.sciencedirect.com/science/article/pii/S004578250000253X

Borja, R. I., Song, X., Rechenmacher, A. L., Abedi, S., Wu, W., Jan. 2013. Shear band in sand with spatially varying density. Journal of the Mechanics and Physics of Solids 61 (1), 219–234.
URL http://www.sciencedirect.com/science/article/pii/S0022509612001524

Boussetta, R., Coupez, T., Fourment, L., 2006. Adaptive remeshing based on a posteriori error estimation for forging simulation. Computer Methods in Applied Mechanics and Engineering 195 (4849), 6626 – 6645, computational Metal Forming.
URL http://www.sciencedirect.com/science/article/pii/S0045782505004780

Camacho, G., Ortiz, M., 1996. Computational modelling of impact damage in brittle materials. International Journal of Solids and Structures 33 (2022), 2899 – 2938.
URL http://www.sciencedirect.com/science/article/pii/0020768395002553

Carol, I., Prat, P., Lpez, C., 1997. Normal/shear cracking model: Application to discrete crack analysis. Journal of Engineering Mechanics 123 (8), 765–773.
URL http://dx.doi.org/10.1061/(ASCE)0733-9399(1997)123:8(765)

Chang, S.-H., Lee, C.-I., Jeon, S., 2002. Measurement of rock fracture toughness under modes i and {II} and mixed-mode conditions by using disc-type specimens. Engineering Geology 66 (12), 79 – 97.
URL http://www.sciencedirect.com/science/article/pii/S0013795202000339

Chen, L., Rabczuk, T., Bordas, S., Liu, G., Zeng, K., Kerfriden, P., 2012. Extended finite element method with edge-based strain smoothing (esm-xfem) for linear elastic crack growth. Computer Methods in Applied Mechanics and Engineering 209212, 250 – 265.
URL http://www.sciencedirect.com/science/article/pii/S0045782511002684

Chen, Q., Andrade, J. E., Samaniego, E., Aug. 2011. AES for multiscale localization modeling in granular media. Computer Methods in Applied Mechanics and Engineering 200 (33-36), 2473–2482.
URL http://linkinghub.elsevier.com/retrieve/pii/S0045782511001630

Cusatis, G. ., Rezakhani, R. ., Alnaggar, M. ., Zhou, X. ., Pelessone, D. ., 2014. Multiscale computational models for the simulation of concrete materials and structures. In: Bcanic, N., Mang, H., Meschke, G., de Borst, R. (Eds.), Computational Modelling of Concrete Structures. Taylor & Francis, London, p. 2338.

de Borst, R., Remmers, J. J., Needleman, A., 2006. Mesh-independent discrete numerical representations of cohesive-zone models. Engineering Fracture Mechanics 73 (2), 160 – 177, advanced Fracture Mechanincs for Life Safety Assessments.
URL http://www.sciencedirect.com/science/article/pii/S0013794405001852

DorMohammadi, H., Khoei, A., Jan. 2008. A three-invariant cap model with isotropickinematic hardening rule and associated plasticity for granular materials. International Journal of Solids and Structures 45 (2), 631–656.
URL http://www.sciencedirect.com/science/article/pii/S0020768307003460

Duflot, M., 2007. A study of the representation of cracks with level sets. INTERNATIONAL JOURNAL FOR NUMERICAL METHODS IN ENGINEERING 70 (11), 1261–1302.

Dugdale, D., 1960. Yielding of steel sheets containing slits. Journal of the Mechanics and Physics of Solids 8 (2), 100 – 104.
URL http://www.sciencedirect.com/science/article/pii/0022509660900132

Erarslan, N., Williams, D. J., 2012. Experimental, numerical and analytical studies on tensile strength of rocks. International Journal of Rock Mechanics and Mining Sciences 49 (0), 21 – 30.
URL http://www.sciencedirect.com/science/article/pii/S1365160911001924

Erdogan, F., Sih, G., 1963. On the crack extension in plates under plane loading and transverse shear. ASME. J. Basic Eng. 85 (4), 519–525.

Espinosa, H. D., Zavattieri, P. D., 2003. A grain level model for the study of failure initiation and evolution in polycrystalline brittle materials. part i: Theory and numerical implementation. Mechanics of Materials 35 (36), 333 – 364.
URL http://www.sciencedirect.com/science/article/pii/S0167663602002855

Flores, E. S., Saavedra, K., Hinojosa, J., Chandra, Y., Das, R., 2015. Multi-scale modelling of rolling shear failure in cross-laminated timber structures by homogenisation and cohesive zone models. International Journal of Solids and Structures, –.
URL http://www.sciencedirect.com/science/article/pii/S0020768315004898

Fossum, A. F., Brannon, R. M., 2004. The Sandia GeoModel: theory and user's guide. SAND report August, Sandia National Laboratories.

Foster, C., Regueiro, R., Fossum, A., Borja, R., Dec. 2005. Implicit numerical integration of a three-invariant, isotropic/kinematic hardening cap plasticity model for geomaterials. Computer Methods in Applied Mechanics and Engineering 194 (50-52), 5109–5138.
URL http://linkinghub.elsevier.com/retrieve/pii/S0045782505000022

Foster, C. D., Borja, R. I., Regueiro, R. A., Oct. 2007. Embedded strong discontinuity finite elements for fractured geomaterials with variable friction. International Journal for Numerical Methods in Engineering 72 (5), 549–581.
URL http://doi.wiley.com/10.1002/nme.2020

Gamnitzer, P., Hofstetter, G., 2015. A smoothed cap model for variably saturated soils and its robust numerical implementation. International Journal for Numerical and Analytical Methods in Geomechanics 39 (12), 1276–1303, nag.2352.
URL http://dx.doi.org/10.1002/nag.2352

Galvez, J., Cervenka, J., Cendon, D., Saouma, V., 2002. A discrete crack approach to normal/shear cracking of concrete. Cement and Concrete Research 32 (10), 1567 – 1585.
URL http://www.sciencedirect.com/science/article/pii/S0008884602008256

Grueschow, E., Rudnicki, J. W., Aug. 2005. Elliptic yield cap constitutive modeling for high porosity sandstone. International Journal of Solids and Structures 42 (16-17), 4574–4587.
URL http://linkinghub.elsevier.com/retrieve/pii/S0020768305000533

Gupta, V., Duarte, C., Babuka, I., Banerjee, U., 2015. Stable {GFEM} (sgfem): Improved conditioning and accuracy of gfem/xfem for three-dimensional fracture mechanics. Computer Methods in Applied Mechanics and Engineering 289, 355 – 386.
URL http://www.sciencedirect.com/science/article/pii/S0045782515000341

Haeri, H., Shahriar, K., Marji, M. F., Moarefvand, P., 2014. Experimental and numerical study of crack propagation and coalescence in pre-cracked rock-like disks. International Journal of Rock Mechanics and Mining Sciences 67 (0), 20 – 28.
URL http://www.sciencedirect.com/science/article/pii/S136516091400029X

Haghighat, E., Pietruszczak, S., 2015. On modeling of discrete propagation of localized damage in cohesive-frictional materials. International Journal for Numerical and Analytical Methods in Geomechanics, n/a–n/a.
URL http://dx.doi.org/10.1002/nag.2368

Hill, R., 1962. Acceleration waves in solids. Journal of the Mechanics and Physics of Solids 10 (1), 1 – 16.
URL http://www.sciencedirect.com/science/article/pii/0022509662900248

Hussain, M., Pu, S., Underwood, J., 1974. Strain energy release rate for a crack under combined mode i and mode ii. In: Fracture Analysis, ASTM STP 560. American Society for Testing and Materials. pp. 2–28.

Jaeger, J. C., Cook, N. G., Zimmerman, R., 2009. Fundamentals of rock mechanics. John Wiley & Sons.

Khan, K., Al-Shayea, N. A., July 2000. Effect of specimen geometry and testing method on mixed mode iii fracture toughness of a limestone rock from saudi arabia. Rock Mechanics and Rock Engineering 33 (3), 179–206.

Kishen, J., Singh, K. D., 2001. Stress intensity factors based fracture criteria for kinking and branching of interface crack: application to dams. Engineering Fracture Mechanics 68 (2), 201 – 219.
URL http://www.sciencedirect.com/science/article/pii/S0013794400000916

Kohler, R., Hofstetter, G., Jun. 2008. A cap model for partially saturated soils. International Journal for Numerical and Analytical Methods in Geomechanics 32 (8), 981–1004.
URL http://doi.wiley.com/10.1002/nag.658

Kourkoulis, S., Markides, C., Chatzistergos, P., 2012. The brazilian disc under parabolically varying load: Theoretical and experimental study of the displacement field. International Journal of Solids and Structures 49 (78), 959 – 972.
URL http://www.sciencedirect.com/science/article/pii/S0020768312000169

Kramer, R., Bochev, P., Siefert, C., Voth, T., 2013. An extended finite element method with algebraic constraints (xfem-ac) for problems with weak discontinuities. Computer Methods in Applied Mechanics and Engineering 266, 70 – 80.
URL http://www.sciencedirect.com/science/article/pii/S0045782513001898

Linder, C., Zhang, X., 2014. Three-dimensional finite elements with embedded strong discontinuities to model failure in electromechanical coupled materials. Computer Methods in Applied Mechanics and Engineering 273, 143 – 160.
URL http://www.sciencedirect.com/science/article/pii/S0045782514000346

Liu, Y., Sun, W., Yuan, Z., Fish, J., 2015. A nonlocal multiscale discrete-continuum model for predicting mechanical behavior of granular materials. International Journal for Numerical Methods in Engineering, n/a–n/aNme.5139.
URL http://dx.doi.org/10.1002/nme.5139

Lu, G., Fall, M., 2015. A coupled chemo-viscoplastic cap model for simulating the behavior of hydrating cemented tailings backfill under blast loading. International Journal for Numerical and Analytical Methods in Geomechanics, In press.
URL http://dx.doi.org/10.1002/nag.2475

Maligno, A., Rajaratnam, S., Leen, S., Williams, E., 2010. A three-dimensional (3d) numerical study of fatigue crack growth using remeshing techniques. Engineering Fracture Mechanics 77 (1), 94 – 111.
URL http://www.sciencedirect.com/science/article/pii/S0013794409002938

Mohammadi, S., 2008. The Extended Finite Element Method for Fracture Analysis of Structures. Blackwell Publishing, Oxford, UK.

Motamedi, M. H., Foster, C. D., 2015. An improved implicit numerical integration of a non-associated, three-invariant cap plasticity model with mixed isotropickinematic hardening for geomaterials. International Journal for Numerical and Analytical Methods in Geomechanics, n/a–n/a.
URL http://dx.doi.org/10.1002/nag.2372

Oliver, J., Caicedo, M., Roubin, E., Huespe, A., Hernndez, J., 2015. Continuum approach to computational multiscale modeling of propagating fracture. Computer Methods in Applied Mechanics and Engineering 294, 384 – 427.
URL http://www.sciencedirect.com/science/article/pii/S0045782515001851

Oliver, J., Huespe, A., Blanco, S., Linero, D., 2006a. Stability and robustness issues in numerical modeling of material failure with the strong discontinuity approach. Computer Methods in Applied Mechanics and Engineering 195 (52), 7093 – 7114, computational Modelling of Concrete.
URL http://www.sciencedirect.com/science/article/pii/S0045782505003920

Oliver, J., Huespe, A., Snchez, P., 2006b. A comparative study on finite elements for capturing strong discontinuities: E-fem vs x-fem. Computer Methods in Applied Mechanics and Engineering 195 (3740), 4732 – 4752, john H. Argyris Memorial Issue. Part I.
URL http://www.sciencedirect.com/science/article/pii/S0045782505005049

Ortiz, M., Pandolfi, A., 1999. Finite-deformation irreversible cohesive elements for three-dimensional crack-propagation analysis. International Journal for Numerical Methods in Engineering 44 (9), 1267–1282.
URL http://dx.doi.org/10.1002/(SICI)1097-0207(19990330)44:9<1267::AID-NME486>3.0.CO;2-7

Park, K., Paulino, G., 2013. Cohesive zone models: A critical review of traction-separation relationships across fracture surfaces. ASME. Applied Mechanics Review 64 (6).

Parvaneh, S., Foster, C., 2016. On numerical aspects of different updating schedules for tracking fracture path in strain localization modeling. Engineering Fracture Mechanics 152, 26–57.

Pietruszczak, S., Mroz, Z., 2001. On failure criteria for anisotropic cohesive-frictional materials. International Journal for Numerical and Analytical Methods in Geomechanics 25 (5), 509–524.
URL http://dx.doi.org/10.1002/nag.141

Rahman, M., Hossain, M., Crosby, D., Rahman, M., Rahman, S., 2002. Analytical, numerical and experimental investigations of transverse fracture propagation from horizontal wells. Journal of Petroleum Science and Engineering 35 (34), 127 – 150.
URL http://www.sciencedirect.com/science/article/pii/S092041050200236X

Regueiro, R. A., Foster, C. D., Feb. 2011. Bifurcation analysis for a rate-sensitive, non-associative, three-invariant, isotropic/kinematic hardening cap plasticity model for geomaterials: Part I. Small strain. International Journal for Numerical and Analytical Methods in Geomechanics 35 (2), 201–225.
URL http://doi.wiley.com/10.1002/nag.907

Rice, J., Rudnicki, J., 1980. A note on some features of the theory of localization of deformation. International Journal of Solids and Structures 16 (7), 597 – 605.
URL http://www.sciencedirect.com/science/article/pii/0020768380900190

Rinehart, A. J., Bishop, J. E., Dewers, T., 2015. Fracture propagation in indiana limestone interpreted via linear softening cohesive fracture model. Journal of Geophysical Research: Solid Earth 120 (4), 2292–2308, 2014JB011624.
URL http://dx.doi.org/10.1002/2014JB011624

Roth, S.-N., Lger, P., Soulamani, A., 2015. A combined xfemdamage mechanics approach for concrete crack propagation. Computer Methods in Applied Mechanics and Engineering 283 (0), 923 – 955.
URL http://www.sciencedirect.com/science/article/pii/S0045782514004137

Rubin, A. M., 1993. Tensile fracture of rock at high confining pressure: Implications for dike propagation. Journal of Geophysical Research: Solid Earth 98 (B9), 15919–15935.
URL http://dx.doi.org/10.1029/93JB01391

Rudnicki, J., Rice, J., 1975. Conditions for the localization of deformation in pressure-sensitive dilatant materials. Journal of the Mechanics and Physics of Solids 23 (6), 371 – 394.
URL http://www.sciencedirect.com/science/article/pii/0022509675900010

Sancho, J. M., Planas, J., Galves, J. C., Reyes, E., Cendon, D. A., 2006. An embedded cohesive crack model for finite element analysis of mixed mode fracture of concrete*. Fatigue & Fracture of Engineering Materials & Structures 29 (12), 1056–1065.
URL http://dx.doi.org/10.1111/j.1460-2695.2006.01076.x

Scheider, I., Brocks, W., 2003. Simulation of cupcone fracture using the cohesive model. Engineering Fracture Mechanics 70 (14), 1943 – 1961, cohesive Models.
URL http://www.sciencedirect.com/science/article/pii/S0013794403001334

Shen, Y., Lew, A. J., 2014. A locking-free and optimally convergent discontinuous-galerkin-based extended finite element method for cracked nearly incompressible solids. Computer Methods in Applied Mechanics and Engineering 273, 119 – 142.
URL http://www.sciencedirect.com/science/article/pii/S0045782514000309

Sih, G., 1974. Strain-energy-density factor applied to mixed mode crack problems. International Journal of Fracture 10 (3), 305–321.
URL http://dx.doi.org/10.1007/BF00035493

Simo, J. C., Oliver, J., Armero, F., 1993. An analysis of strong discontinuities induced by strain-softening in rate-independent inelastic solids. Computational Mechanics 12 (5), 277–296.

Sun, W., Chen, Q., Ostien, J. T., Nov. 2013. Modeling the hydro-mechanical responses of strip and circular punch loadings on water-saturated collapsible geomaterials. Acta Geotechnica.
URL http://link.springer.com/10.1007/s11440-013-0276-x

Tjioe, M., Borja, R. I., 2016. Pore-scale modeling of deformation and shear band bifurcation in porous crystalline rocks. International Journal for Numerical Methods in Engineering, n/a–n/aNme.5208.
URL http://dx.doi.org/10.1002/nme.5208

Tonge, A. L., Ramesh, K., 2016. Multi-scale defect interactions in high-rate brittle material failure. part i: Model formulation and application to {ALON}. Journal of the Mechanics and Physics of Solids 86, 117 – 149.
URL http://www.sciencedirect.com/science/article/pii/S0022509615302003

Tvergaard, V., 1990. Effect of fibre debonding in a whisker-reinforced metal. Materials Science and Engineering: A 125 (2), 203 – 213.
URL http://www.sciencedirect.com/science/article/pii/0921509390901708

Weed, D. A., Foster, C. D., Motamedi, M. H., 2015. A combined opening-sliding formulation for use in modeling geomaterial deformation and fracture patterns. Acta Geotechnica, Under review.

Whittaker, R., Singh, R., Sun, G., 1992. Rock fracture Mechanics: Principles, Design and Applications. Elsevier Science Ltd.

Wu, J.-Y., 2011. Unified analysis of enriched finite elements for modeling cohesive cracks. Computer Methods in Applied Mechanics and Engineering 200 (4546), 3031 – 3050.
URL http://www.sciencedirect.com/science/article/pii/S0045782511001812

Wu, J.-Y., Li, F.-B., Xu, S.-L., 2015. Extended embedded finite elements with continuous displacement jumps for the modeling of localized failure in solids. Computer Methods in Applied Mechanics and Engineering 285, 346 – 378.
URL http://www.sciencedirect.com/science/article/pii/S0045782514004381

Xu, X. P., Needleman, A., 1993. Void nucleation by inclusion debonding in a crystal matrix. Modelling and Simulation in Materials Science and Engineering 1 (2), 111.
URL http://stacks.iop.org/0965-0393/1/i=2/a=001

Yao, Y., 2012. Linear elastic and cohesive fracture analysis to model hydraulic fracture in brittle and ductile rocks. Rock Mechanics and Rock Engineering 45 (3), 375–387.
URL http://dx.doi.org/10.1007/s00603-011-0211-0

Zhang, Y., Lackner, R., Zeiml, M., Mang, H. A., 2015. Strong discontinuity embedded approach with standard {SOS} formulation: Element formulation, energy-based crack-tracking strategy, and validations. Computer Methods in Applied Mechanics and Engineering 287, 335 – 366.
URL http://www.sciencedirect.com/science/article/pii/S0045782515000390